Reliable chiral recognition with an optoelectronic nose

Pierre Maho, Cyril Herrier, Thierry Livache, Guillaume Rolland, Pierre Comon, Simon Barthelme

Reliable chiral recognition with an electronic nose

Pierre Maho[a], Cyril Herrier[b], Thierry Livache[b], Guillaume Rolland[b], Pierre Comon[a], Simon Barthelmé[a]

[a] *CNRS, GIPSA-Lab, Univ. Grenoble Alpes, F-38000 Grenoble, France*
[b] *Aryballe, 38000 Grenoble, France*

Abstract

Chiral discrimination is a key problem in analytical chemistry. It is generally performed using expensive instruments or highly-specific miniaturized sensors. An electronic nose is a bio-inspired instrument capable after training of discriminating a wide variety of analytes. However, generality is achieved at the cost of specificity which makes chiral recognition a challenging task for this kind of device. Recently, a peptide-based optoelectronic nose which can board up to hundreds of different sensing materials has shown promising results, especially in terms of specificity. In line with these results, we describe here its use for chiral recognition. This challenging task requires care, especially in terms of statistical reliability and experimental confounds. For these reasons, we set up an automatic gas sampling system and recorded data over two long sessions, taking care to exclude possible confounds. Two couples of chiral molecules, namely (R) and (S) Limonene and (R) and (S) Carvone, were tested and several statistical analyses indicate the almost perfect discrimination of their two enantiomers. A method to highlight discriminative sensing materials is also proposed and shows that successful discrimination is likely achieved using just a few peptides.

Keywords: peptides, electronic noses, chirality, enantioselectivity, surface plasmon resonance imaging

1. Introduction

Chiral discrimination is a fascinating aptitude of natural olfaction [4], one that is hard to replicate in machines. Conventional methods such as liquid chromatography are accurate and reliable but are complex, time-consuming and expensive. In contrast, miniaturized highly-specific sensors such as molecularly imprinted polymer sensors can be used as fast, repeatable, low-cost and portable instruments [14, 26, 24]. However, this type of sensors are often designed for a chiral pair, preventing them from being used for other analyses.

As an alternative, electronic noses (eNoses) are highly interesting, especially for their versatility. The technology is broadly inspired from mammalian olfaction [20] and mainly based on a cross-sensitive chemical sensor array [1]. In practice, a database of signatures for targeted molecules is generated and machine learning algorithms are used to recognize them. One of the main advantages of using this kind of devices compared to others is that it can discriminate among a broad variety of molecules. In fact, an eNose tries to be a universal device. This weak specificity of eNoses is a strength and a requirement, but makes the chiral recognition a really challenging task. The enantioselectivity of eNoses has been assessed for some technologies such as TGS sensors [7] or DNA coated sensors [12, 13]. But these results can be statistically unreliable due to datasets which are too small. In fact, criticisms concerning the experimental methodology have already been expressed to the field [5, 15]. Coupled with the typically limited number of chemical sensors used [21], this explain why despite the promise of the technology, electronic noses have not been widely adopted. In this article, we propose an experimental methodology to achieve this challenging task, which could be replicated to provide more reliable and realistic results.

Our group recently described a new optoelectronic nose able to board up to hundreds of different sensing materials without increasing system complexity [6]. In this work, peptides were used as sensing materials due to their close connection to olfactory receptors [17, 25]. They were deposited on the golden surface of a prism and Surface Plasmon Resonance imaging (SPRi) was used to record chemical interaction in real-time. This transduction mechanism is briefly described in Figure 1b. Brenet and coworkers demonstrated that the developed eNose is a promising new analytical tool enabling the discrimination of both different and similar molecules up to a single carbon atom [6].

In this article, we investigate the enantioselectivity of this new technology with a *commercial* version of the eNose described by Brenet and coworkers [6]. Formally, we expect that the discrimination between two mirror molecules, or enantiomers, is possible, thanks to the potential enantioselectivity of peptides used in the device [28]. Indeed, peptides are chiral in essence and previous works with specific sensors already reported their enantioselectivity [16]. To take into account the criticisms addressed to the field [5, 15], we took care to design an experimental methodology which has a threefold goal: minimize statistical error, minimize potential experimental confounds and keep a realistic gas sampling system. To achieve the first objective, we used an automatic sampling system which can generate substantial datasets. The second

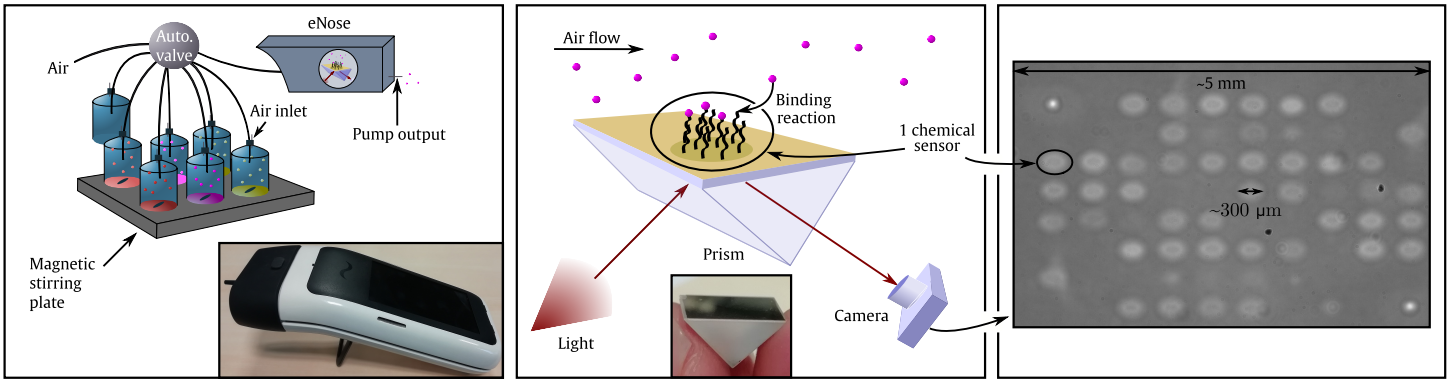

(a) Experimental setup (b) Working principle (c) A raw image

Figure 1: (a) The valve is programmed to start with the air line (reference acquisition). Then, at t_s, the valve switches to line i (analyte injection). At t_e, it goes back to the air line (recovering). The process is repeated for the line $i+1$ and so on. (b) Working principle of the optoelectronic nose based on SPRi. Briefly, a light is sent, reflected by the surface and caught by a simple camera. When a binding reaction occurs with the molecule, this changes the refraction index leading to a change in reflectivity. (c) Raw image of the prism surface with some dimensions. Light areas stand for the functionalized surface.

objective is achieved by repeating the experiment across two different sessions, controlling various factors. For the last objective, we used the evaporation of the chemical compounds in liquid phase to be closer to an industrial application.

With this methodology, we confirm that the new eNose is able to discriminate between molecules which differ strongly. More importantly, we also show its ability to discriminate between two enantiomers by way of two examples, namely the mirror images of Carvone and Limonene. These results are supported by two reliable analyses. The first one, namely an intra-session analysis, shows a nearly perfect discrimination when we train and test from samples from the same experiment. The second one, namely an inter-session analysis, shows a stronger result where we can learn from samples from one dataset (one session) and still almost perfectly discriminate the samples from a new experiment which reuses the setup (meaning another session). In this article, we also propose a metric which can be used to highlight the most discriminative sensing materials. Another key point of this study is that the eNose has not been tuned for this discrimination task.

2. Material and Methods

2.1. Experimental setup

2.1.1. Chemical compounds

All the products were purchased from Sigma-Aldrich: Butanol, mineral oil, (R)-Carvone pure at 99.4%, (S)-Carvone pure at 99.3%, (R)-Limonene pure at 98.4% and (S)-Limonene pure at 97.9%. The purity of each enantiomer comes from the certificate of analysis of Sigma-Aldrich. Due to the volatility of Butanol and to the duration of the experiments, we conducted a volumetric dilution at 25% in mineral oil to avoid exhaustion. This dilution is only conducted on Butanol and the other chemical compounds are left pure and used as received without further purification.

The purity degree of the samples is in line with previous studies (and even better) using the same compounds [7].

2.1.2. Optoelectronic nose

The eNose is provided by Aryballe and more details about the device can be found in [6]. Sensing materials are mainly peptides which are fixed on the gold surface of a prism (see supplementary materials S1 for some details about the source and the deposition of peptides). During an acquisition, the analyte is brought above the gold surface by a flow of air using a pump (in this study, at 63 mL/min). The analyte can then interact with the sensing material through a reversible binding reaction. This reaction is both dependent on the analyte and on the sensing material. Thus, different sensing materials will lead to different chemical reactions, creating a chemical "signature" of the analyte. Since different analytes lead to different chemical reactions, and thus different signatures, we are able to recognize analytes. Here, 19 different sensing materials are deposited on the surface of the prism, 17 of them being peptides. The two remaining sensing materials are achiral molecules and are used as a control for the study. Each sensing material is repeated 3 or 4 times on the surface, leading to a cross-sensitive chemical sensor array of 59 elements.

The binding reactions at the surface are measured using Surface Plasmon Resonance imaging (SPRi). Briefly, light is sent, reflected by the surface and caught by a simple optical camera. When a binding reaction occurs with the analyte, this changes the refraction index (more light is reflected). The changes in reflectivity are caught by the camera, which thus records in real-time the binding reactions. A representation of the working principle is presented in Figure 1b. A real image of the prism surface is reported in Figure 1c.

2.1.3. Gas sampling system

In this study, we use an automatic gas sampling system to create substantial data sets ($\geq$100 samples/class). The main part of this system is an automatic valve represented in Figure 1a. One of the 8 lines is booked for ambient air which is used as our reference gas. Four lines are allocated

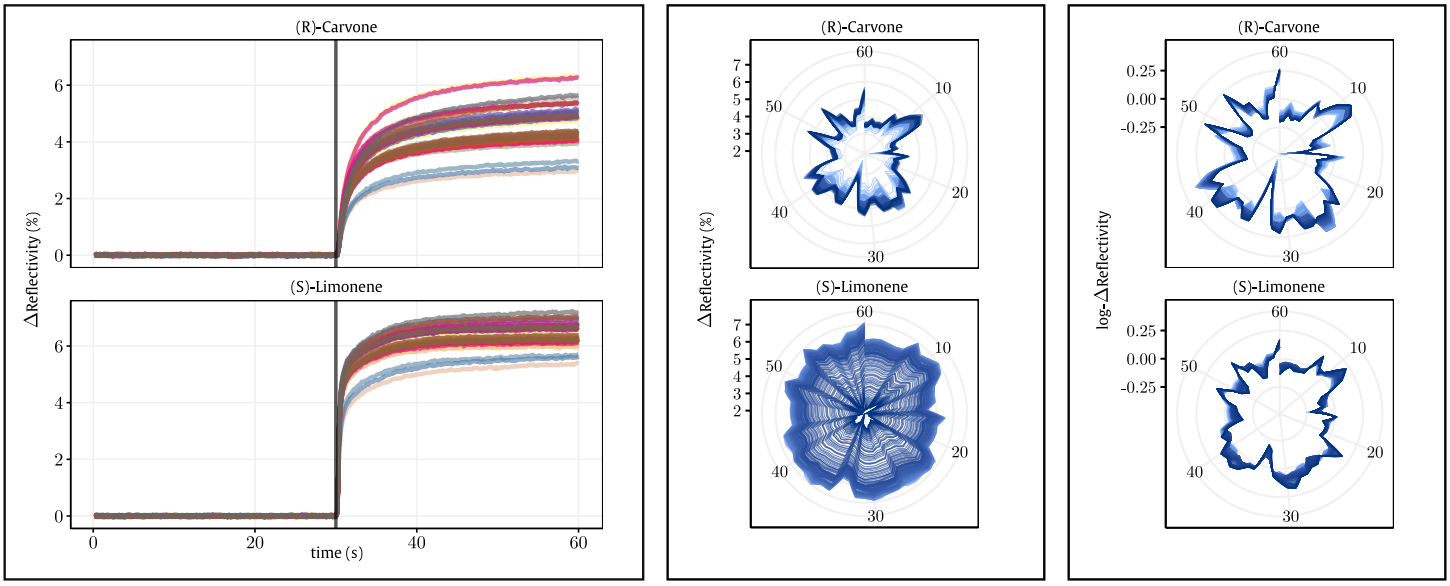

(a) Time series (b) Raw signatures (c) Normalized signatures

Figure 2: (a) Example of time series obtained for (R)-Carvone and (S)-Limonene. A vertical line indicates the molecule injection. It corresponds to a single measurement, and the baseline has been subtracted. (b) Raw signatures (integration of the adsorption part, over the 30 s after injection in (a)) in polar coordinates (angle for spot number and radius for amplitude). Color gradation stands for the cycle number (the initial cycle is the lighter, meaning the first measurements), showing for example the gradual exhaustion of Limonene during Session 2. (c) Normalized signatures according to (1): repeatability is visibly increased (compared to unnormalized signatures in (b)).

for two pairs of enantiomers. We choose the two chiral forms of Carvone and Limonene. A potential concern is that by using the instrument near its discriminability limit, we may be amplifying potential confounds which could lead to artificial discriminability between vials rather than products (no two vials are exactly equal). As a control, an achiral molecule, Butanol, is added in two different vials and is placed in the valve's cycle between two mirror molecules.

All lines except the reference line are inserted in 50 mL vials, which are sealed with a Teflon-coated silicon septum and filled with a liquid solution of each analyte. The vials containing analytes are agitated using a magnetic stir bar to homogenize the headspace and a small polyether ether ketone (PEEK) tube is used to balance the pressure inside the vials. The fluidic system is made of peek tubing. Each gas line has the same tube length. The time segmentation used is as follows: 30 sec for the reference gas (*ie* ambient air), 30 sec for analyte injection and 5 min for desorption. Only the two first phases are recorded and the third one is deliberately long, as a precaution. Consequently, a valve's cycle lasts 42 min, corresponding to 7 measurements. A complete measurement for (S)-Limonene including the desorption phase is reported in supplementary materials S2.

The automatic setup can generate a significant number of samples, but all samples follow the same running order. This could induce another confound, specifically a memory effect [9] which can lead to artificial discrimination only related to the running order. To overcome this issue, we switch the position of the enantiomers across 2 sessions. The experimental protocol is presented in Table 1. Between sessions, we emphasize that all the vials are changed for Session 2 and filled

	Session 1		Session 2	
Line	Molecule	V (mL)	Molecule	V (mL)
①	Air (baseline)	-	Air (baseline)	-
②	(R)-Limonene	0.4	(S)-Carvone	0.150
③	Butanol	1.6 at 25%	Butanol	1.6 at 25%
④	(S)-Limonene	0.4	(R)-Carvone	0.150
⑤	Butanol	1.6 at 25%	Butanol	1.6 at 25%
⑥	(R)-Carvone	0.4	(S)-Limonene	0.150
⑦	Empty vial	-	Empty vial	-
⑧	(S)-Carvone	0.4	(R)-Limonene	0.150

Table 1: Experimental protocol reporting the lines allocation for each session.

with new products taken from the same stock solutions as in Session 1. There is a difference in liquid volume between the two sessions, which adds another source of variability. Finally, we stress that the whole setup is left at room conditions during the 2 sessions which can introduce some temperature and humidity variations. In this way, more realistic data can be generated.

Session 1 lasted ∼88 hours, providing 125 samples/molecule and Session 2 lasted ∼182 hours for 260 samples/molecule, both run without interruption. Session 1 and Session 2 are separated by a single day and the total duration of the experiments is ∼13 days.

2.2. Data analysis

2.2.1. Feature extraction

Raw data is a collection of images (such the one presented in Figure 1c) which report in real-time, at a frame rate of 5 Hz, the binding reactions occurring at the surface of the prism,

during an acquisition. From these images, a binary mask is applied to extract only the areas where sensing materials have been deposited (light areas in Figure 1c). In each area, or spot, we average all the pixels and the resulting values are converted to a percentage of reflectivity $R(\%)$ by means of an external reference [3]. Then, for each spot individually, we subtract the reference gas value (computed by averaging the first 25 sec of signal) to remove, at least partially, some drift due to a reference change [8]. The remaining $\Delta R(\%)$ signals are represented in Figure 2a and show the fast response of the eNose to the molecules, or analytes, while already emphasizing the diversity across sensing materials, with different peptides responding differently. From these time series, whose general shape is well-known in the literature, one or two features are generally extracted. The most common one is the steady state value [27]. This value is chemically justified since a single time series corresponds to the binding reaction between the sensing material and the analyte. This reaction is likely to reach an equilibrium phase, stabilizing the response around a given value. However, due to the schedule we used, some analytes reach equilibrium while others do not. As an alternative to steady-state values, we propose to integrate the signal over the entire adsorption part. We retain the value of the integral as a feature (*e.g.* the integration over the 30 seconds after the molecule injection). Each spot provides a feature, and this procedure therefore gives us a vector $y_{rn} \in \mathbb{R}^P$, with P the number of spots, for the measure of the analyte r during a valve cycle n.

2.2.2. Normalization

All measures from Session 2 are represented in polar coordinates in Figure 2b. On the same figure, we can easily see the exhaustion occurring over time, especially for Limonene, leading to a change in concentration, which in turn results in a decrease in reflectivity. As this study is interested in qualitative results, variations in concentration cause undesirable variations. To eliminate these variations, we normalize y_{rn} as follows, where subscript p refers to the spot:

$$\tilde{y}_{prn} = \log(y_{prn}) - \frac{1}{P}\sum_{i=1}^{P} \log(y_{irn}) \qquad (1)$$

The normalization (1) implies that measurements scale linearly with analyte concentration. Although clearly an approximation, it has always worked well in practice and has some theoretical backing (see supplementary materials S3 for demonstration). The normalized data of the Session 2 is represented in Figure 2c and clearly demonstrate the increased repeatability of the measures, even if some time-related variations remain.

2.3. Discrimination of different analytes

Before studying chiral recognition in detail, we confirm that the eNose can successfully discriminate between different molecules, replicating previous studies. To this end, we temporarily erase the chiral labels in the database, for example (R)-Carvone and (S)-Carvone are now just summarized as "Carvone". In this scenario, we have 250 samples/class for the Session 1 and 520 samples/class for the Session 2 and the data sets include the two Terpenes, namely Carvone and Limonene, and also Butanol. To assess discriminative power, we first reduce the dimensionality by projecting the data on the 5 first Principal directions and then perform a classical 10-fold cross validation with a linear Support Vector Machine (SVM) to estimate the classification rate. This process is applied session-by-session. The results give without difficulty a perfect classification score for both sessions and are consequently in agreement with previous work [6].

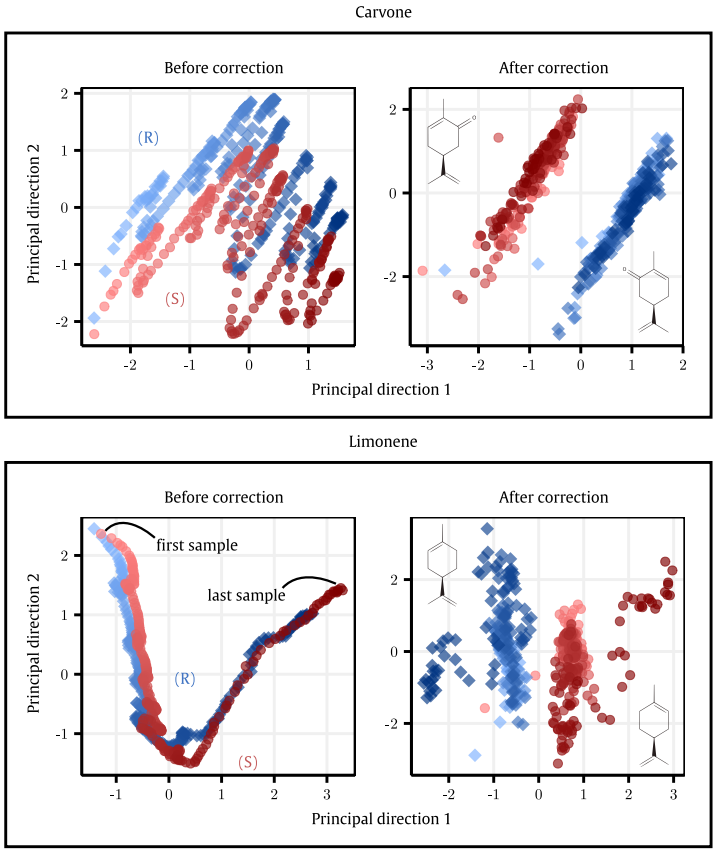

Figure 3: Projection of the data from Session 2 on the 2 first Principal directions, separately for Carvone (top) and Limonene (bottom). On the right, the drift has been corrected, whereas on the left not. Each point corresponds to a measurement such the one in Figure 2a. Cycle number is represented in the color scale (the initial cycle has the lightest colour). The data set used here is from Session 2. The maps have been centered and scaled for easier visualization.

2.4. Intra-session chiral recognition

We now complicate the task and "zoom in" on either Carvone or Limonene by focusing on each chiral pair. We emphasize that the two sessions and the two pairs are processed separately in this section. For visualization, data projected on the two first Principal directions for each chiral molecule are represented in Figure 3 (left panel), only for Session 2.

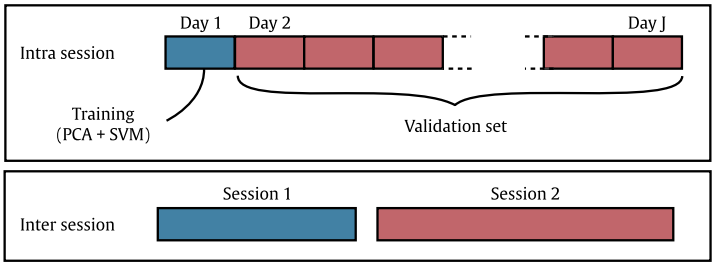

Figure 4: Validation scheme used for assessing drift correction.

	Session	Before correction (%)	After correction (%)
Carvone	1	86.3	98.9
	2	73.8	99.7
Limonene	1	95.7	100
	2	65.3	99.6

Table 2: Comparison with and without drift compensation applied session-by-session. The difference of scores between Session 1 and Session 2 before correction can be explained by the difference of duration. Indeed, Session 2 lasts twice the time of Session 1, thus Session 2 includes more drift.

2.4.1. Drift compensation

The lack of stability over time is clearly perceptible in Figure 3 (left panel). This is of course not unexpected, since chemical sensors are unfortunately prone to drift, and the new eNose is no exception to the rule. Drift can be explained by one or more of the following factors: physical changes in the sensing materials or modifications in the chemical background, or yet changes in the environmental conditions (for instance, the day/night cycle is clearly visible for Carvone in Figure 3) [2]. Drift has been studied many times and many correction methods have been proposed to compensate for it, so that this remains an active research topic [2, 18, 22]. These methods are often based on calibrating compounds, meaning that the drift of some analytes can be known and thus correlated to the drift of others, which are then corrected. Here, our case study is simpler in that we cannot find two other molecules which are more similar than the two we are looking at, namely two enantiomers. Consequently, it is very likely that the 2 molecules will be affected by the same amount and direction of drift. This is even more true due to the experimental setup and to the short time spacing between two enantiomeric samples. Considering these arguments, we propose a simple filtering method to compensate for drift. Our method is closely related to a kind of moving average filter. By considering an already normalized data set, the procedure is as follows: for a given sample taken at time t_0, take all the enantiomeric samples ((R) and (S)) of one chiral analyte recorded in the time window $[t_0 - \Delta t, t_0 + \Delta t]$ ($\Delta t = 5$ hours in this study), compute the averaged signature and subtract it from the given sample. Mathematically, this method removes a drift which is assumed to be additive, equal for the two chiral forms and slowly varying in the time window considered.

2.4.2. Validation method

The success of our method for drift compensation is visible on Figure 3 (right panel). To assess quantitatively both drift compensation and chiral recognition, we use a chronological validation differing from standard cross-validation (similar to the scheme in [18]). Standard cross-validation divides the dataset into random pieces (folds), disregarding temporal order. This enables classifiers to "learn the drift", meaning that they find a linear discriminant that is orthogonal to the drift direction. Instead, we split each session into continuous blocks of one day each. Then, a single one-day block is taken for training (which includes both the estimation of the Principal directions and the fitting of SVM classifier), and all other blocks are used for validation (estimating discrimination performance). This process is repeated for each day and the classification rates are then averaged: this method thus answers the question of how reliable the signatures learned on a single day are, when used on another day (and drift may have occurred in between). The validation scheme is reported in Figure 4. Concerning chiral recognition, classification rates, after correction and averaging across sessions, reach the almost perfect scores of 99.3% and 99.8% respectively for Carvone and Limonene. These scores clearly indicate that the eNose can learn to discriminate the vial containing the left-hand form from the one containing the right-hand form. The comparison of results with and without drift compensation is indicated in Table 2.

2.5. Inter-session chiral recognition

Enantio-discrimination with a non-specific device is a very hard discrimination task, which requires a very sensitive instrument. As a result of the instrument's sensitivity, a successful discrimination could be explained by an experimental artefact instead of an actual discrimination between different analytes. To exclude this possibility, we have carried out several controls which are left in supplementary materials (S4) but we deem necessary to present here an analysis which echoes the previous one.

The two sessions that we have presented so far varied in some of their parameters. As a reminder, there were variations in concentrations, the vials which have been changed and filled with new products (from the same stock solutions), the magnetic stir bars and the running order are not identical from one session to the other. A resulting check is whether one could successfully generalize from one session to the other?

To answer this question, the procedure is as follows: learn to discriminate the 2 mirror molecules using the data from one session and try to classify them in the other session. To clarify, we compute the new representation space (based on PCA) and optimize the SVM from Session 1 and we compute the classification rate obtained for Session 2. This validation methodology is repeated by interchanging the role of each session. The validation scheme is reported in Figure 4.

The projection of samples from Session 2 in the representation space generated by the Session 1 is represented in Figure 5. Again, numerical results follow the visual impression since the averaged classification rate (across the sessions, each one

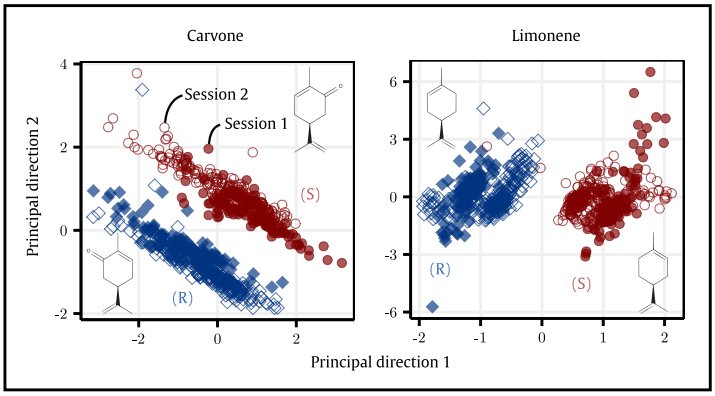

Figure 5: Multi-session representation. The two data sets have been drift compensated beforehand. The Principal directions are learnt from the Session 1 and the data from Session 2 are projected in this subspace. Colors indicate the enantiomer. Solid shape is for Session 1 and hollow shape for Session 2. The maps have been centered and scaled for visual consideration.

taken as the train set for the other) reaches respectively 99.9% for Carvone enantiomers and 99.8% for those of Limonene. These results reduce the likelihood of a memory effect or an artifact-based differentiation.

3. Discussion

From these results, a question remains which is, how can we explain such successful discrimination?

3.1. Vial differentiation

A recent paper warned researchers about the underestimated contamination brought by magnetic stir bars, which are often assumed clean after intensive washing [19], but may retain traces of their previous uses. In fact, the same may hold for every material used in chemical experiments. In our case, these contaminations may mean that the differentiation is artefactual, due to traces left in vials or in the tubing. We define this potential artefactual discrimination as "vial differentiation". Even if the multi-session analysis tends to indicate that it is an unlikely source for our near-perfect classification rates, we describe below an additional control.

In the experimental protocol in Table 1, two vials are booked for the same analyte, namely Butanol. Thus, if there is indeed the possibility for vial differentiation, the samples from these two vials should show it. We propose to look at the Euclidean distances between the samples of two different vials measured during cycle n. Since we have 6 different vials containing analytes, this leads to 15 distances (the number of possible pairs) but only 6 among them are really relevant. For instance, one of these 6 pairs is the pair of (S)-Limonene and (R)-Limonene. Let us note $\tilde{y}_{pn}(R)$ (resp. $\tilde{y}_{pn}(S)$) the normalized response of the chemical sensor p to (R)-Limonene (resp. (S)-Limonene) during cycle n. The Euclidean distance is defined as:

$$d_n(\text{(R)-Limonene}, \text{(S)-Limonene}) = \sqrt{\sum_{p=1}^{P} (\tilde{y}_{pn}(R) - \tilde{y}_{pn}(S))^2}$$

This distance is computed for each cycle n and separately for each session (since the two sessions do not have the same number of samples), without any drift correction, such as not to incorporate any bias. For each session, we average all the distances and compute the standard deviation. Finally, we average all the sessions by weighting with their number of samples. It corresponds to the bar ((S)-Limonene, (R)-Limonene) in Figure 6. The error bar corresponds to the pooled standard deviation. This process is repeated for each relevant pair of vials and results are reported in Figure 6.

This analysis highlights that there is indeed a vial differentiation since the distance separating the clusters of the same analyte (Butanol) in two different vials is not zero. These checks should be considered by future studies, especially when the differences are tiny. In our case, pure vial differentiation is insufficient to explain the distance between chiral samples. Other controls can be found in supplementary information (S4).

3.2. Chemical differentiation

In this section, we proposed a metric for highlighting the most discriminative sensing materials.

Peptides are chiral molecules and are known to be good candidates for the differentiation of two mirror molecules [16]. We sought to verify that it is indeed what drives chiral discrimination in our case, since our instrument also carries 2 achiral sensing materials. To do that, we quantify the discriminative power of each sensing material. Recall that a given sensing material may be used for more than one spot, so that in the following, each sensing material is summarized by the average of its replicas. There are 19 different sensing materials on the device, with 17 of them chiral, and 2 achiral, the latter playing the role of controls. The goal of the analysis is to assess

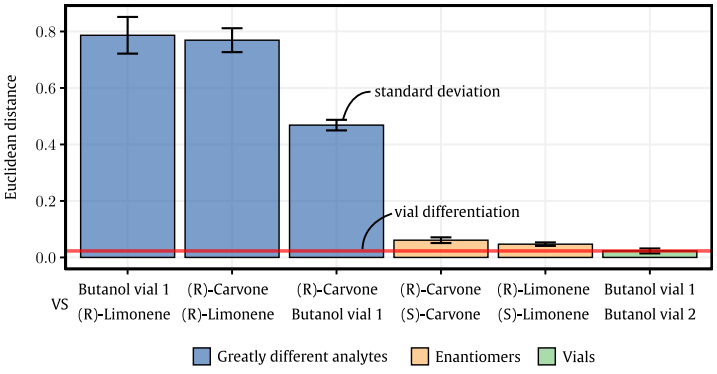

Figure 6: Vial differentiation analysis. We take as our criterion the Euclidean distance between samples from two different vials during the same cycle. These distances are computed for all the cycles of a single session. For each session, we compute the average and the standard deviation. Finally, the bars correspond to the weighted average over sessions and the error bars to the pooled standard deviation

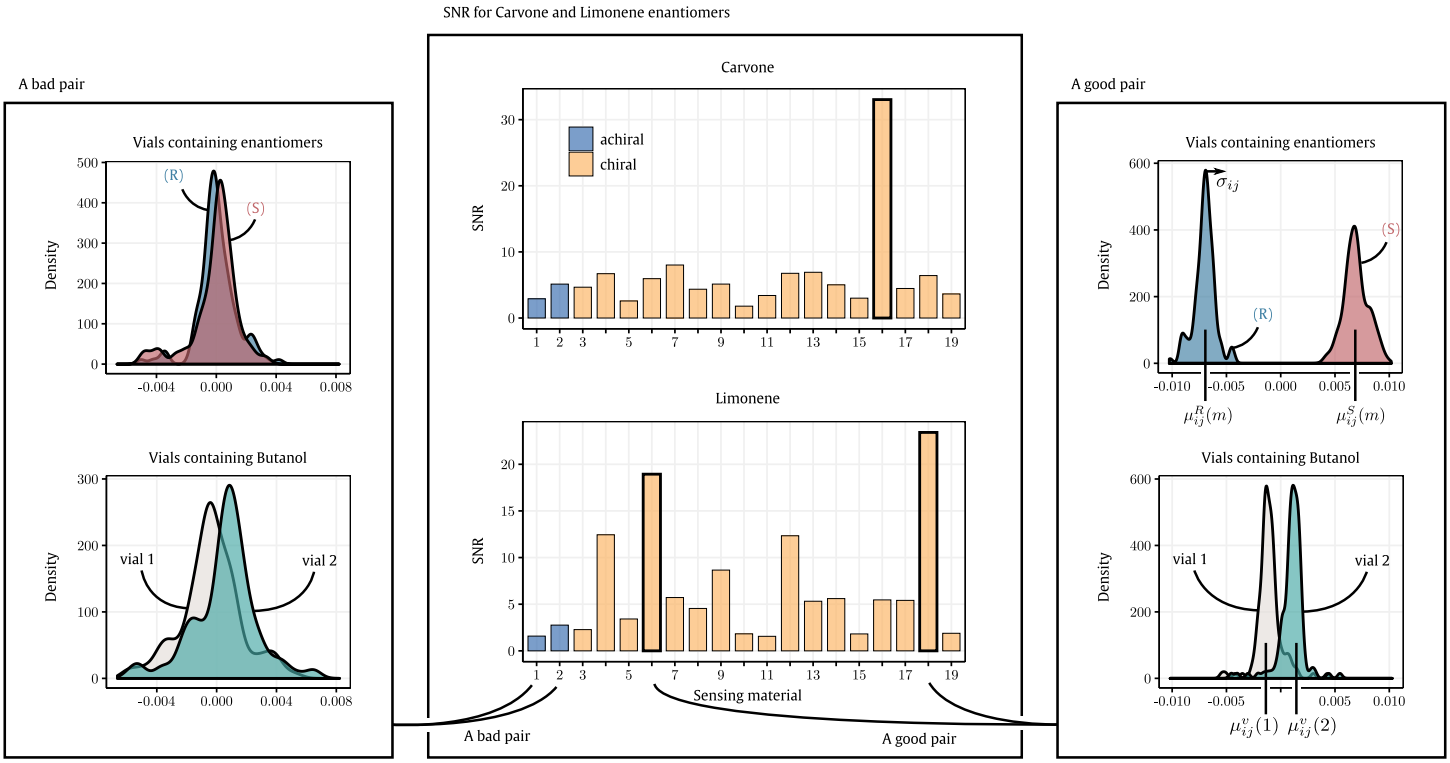

Figure 7: Signal to Noise Ratio used to identify discriminative sensing materials. Middle figure, each bar corresponds to the averaged SNR of one sensing material across all its possible pairs. SNR value is averaged over the two sessions. The colors indicate either the sensing material is chiral (yellow) or achiral (blue). Left and right figures represent respectively the histograms (the data used for illustration is from Session 1) for a bad and a good pair of sensing materials.

which sensing materials drive the discriminative power for the chiral compounds used here.

A simple analysis would look at the sensing materials one-by-one, and see if they can be used *on their own* for chiral discrimination. A problem arises rapidly: the normalization given in (1), compulsory for removing variations in measurements due to variations in concentration, implies the use of several sensing materials. This means we cannot look at sensing materials one-by-one. Another incorrect procedure would be to use all the sensing materials to first normalize and then to look at them one-by-one. This will implicitly introduce a bias invalidating the analysis.

We can illustrate it with a short numerical example using only two sensing materials for discriminating two analytes, say A and B. We assume that sensing material 1 is discriminative whereas sensing material 2 is not. Note c_A and c_B the concentration of A and B during an experiment for which we have the raw responses reported in Table 3a.

Table 3: Numerical example showing the discriminative bias introduced by the normalization.

(a) Raw responses

	To A	To B
y_1	c_A	$2c_B$
y_2	c_A	c_B

(b) Responses after normalization

	To A	To B
$\tilde{y}_1$	0	$\frac{1}{2}\log(2)$
$\tilde{y}_2$	0	$-\frac{1}{2}\log(2)$

Sensing material 2 (with raw response y_2) is clearly not discriminative since it shares the same affinity with A and B, only a difference in concentration would lead to a difference in response. Sensing material 1 (with raw response y_1) is discriminative since its affinity with B is twice greater than with A. To get rid of the variations in concentration, we normalize using Eq. (1), leading to the normalized responses reported in Table 3b.

Eventually, after normalization, sensing material 2 becomes discriminative, but only thanks to the initial discriminative power of sensing material 1. It is not hard to understand that this simple example generalizes to P sensing materials. In fact, only one discriminative sensing material can create discriminative information for all the others.

This bias is inevitable but we can reduce it by only looking at the sensing materials pair-by-pair. In the following, we assume that we have selected a pair of sensing materials, normalized the responses using (1) (for signatures of dimension 2) and corrected the drift. It's interesting to note that since in this case (1) creates a linear dependency between the two dimensions, we have effectively a one-dimensional measurement (S3).

Second, we need to quantify the discriminative power of a given pair of sensing materials. We propose to use a kind of Signal to Noise Ratio (SNR). We define the signal part as the squared distance between (R) centroid $\mu^R \in \mathbb{R}$ and (S) centroid $\mu^S \in \mathbb{R}$; the greater it is, the easier chiral recognition

is. Noise can arguably be measured by the standard deviation σ^2 of the samples (for a given analyte), which quantifies measurement uncertainty. σ^2 is here calculated using samples from the (R) enantiomer (the results do not change if we take the (S) enantiomer). However, the previous section highlighted another kind of noise, namely vial differentiation, which is another source of experimental uncertainty. To incorporate this source of noise into the SNR, we focus again on the two vials containing Butanol (*cf* Table 1). Similarly to the signal estimation, we take as the noise attributed to vial differentiation, the squared distance between the centroid of the first vial $\mu^v(1) \in \mathbb{R}$ and the centroid of the second vial $\mu^v(2) \in \mathbb{R}$. The greater this value is, the more likely it is that discrimination performance is artefactual. Vial noise is then added to measurement noise. For a chiral molecule m and the pair formed by the sensing material i with the sensing material j, this gives:

$$\mathrm{SNR}_{ij}(m) = \frac{(\mu^R_{ij}(m) - \mu^S_{ij}(m))^2}{(\mu^v_{ij}(1) - \mu^v_{ij}(2))^2 + \sigma^2_{ij}} \quad (2)$$

This estimation is computed for all 171 distinct pairs. To make the results more clear, we average the scores for a given sensing material over all pairs in which it appears. The resulting SNR and a graphical explanation are given in Figure 7. The greater the SNR, the more discriminative the sensing material is. Due to confidentiality concerns, the nature of the sensing materials is not given and labels are substituted by arbitrary numbers[1].

We warn that this method does not really correspond to the "true" discriminative power of a sensing material since we are using pairs. However, we believe that this method is sufficient for evaluating which sensing materials are discriminative and which are not. Results show very high scores for sensing material 16 for Carvone and the two sensing materials 6 and 18 for Limonene. These 3 sensing materials could then be replicated multiple times to design a specific instrument to a given chiral pair. Finally, these 3 sensing materials are peptides whereas the two achiral molecules are always among the worst.

4. Conclusion

This paper proposed a robust and statistically reliable methodology based on a realistic gas sampling system and two different sessions over several days of measurement. It demonstrated the ability of a peptide-based optoelectronic nose to tell Limonene and Carvone enantiomers apart, while still retaining enough flexibility to also discriminate between non-enantiomers. A metric has also been proposed to identify the most discriminative sensing materials.

Biological olfaction uses a wider variety of sensing materials (up to 1,000 receptor subtypes, although all may not be used, see [23]) and further development should produce new sensing materials which can be immobilized on the surface to increase the number of olfactory receptors (see [11] for the use of odorant binding proteins and [10] for the use of hairpin DNA). Further studies should be conducted on a wider range of chiral pairs, but also on enantiomeric mixtures. The synthesis of an enantiomer often starts from its racemic mixture and having an inexpensive and flexible device that can measure relative enantiomeric concentrations would be highly valuable for production.

[1]For reproducibility purposes, the instrument can be ordered from Aryballe.

Acknowledgments

This work was supported by the FUI WISE AAP21 minalogic project, BPI (France). This work was also partially supported by MIAI @ Grenoble Alpes (ANR-19-P3IA-0003). The authors would like to acknowledge Etienne Bultel and Johanna Decorps from the start-up Aryballe for their highly valuable help in the generation of the data. The authors would also like to acknowledge Liz Facteau for proofreading the article.

References

[1] Albert, K. J., Lewis, N. S., Schauer, C. L., Sotzing, G. A., Stitzel, S. E., Vaid, T. P., Walt, D. R., Jul. 2000. Cross-Reactive Chemical Sensor Arrays. Chemical Reviews 100 (7), 2595–2626.

[2] Artursson, T., Eklöv, T., Lundström, I., Mårtensson, P., Sjöström, M., Holmberg, M., Sep. 2000. Drift correction for gas sensors using multivariate methods. Journal of Chemometrics 14 (5-6), 711–723.

[3] Bassil, N., Maillart, E., Canva, M., Lévy, Y., Millot, M.-C., Pissard, S., Narwa, R., Goossens, M., Oct. 2003. One hundred spots parallel monitoring of DNA interactions by SPR imaging of polymer-functionalized surfaces applied to the detection of cystic fibrosis mutations. Sensors and Actuators B: Chemical 94 (3), 313–323.

[4] Bentley, R., Sep. 2006. The Nose as a Stereochemist. Enantiomers and Odor. Chemical Reviews 106 (9), 4099–4112.

[5] Boeker, P., Dec. 2014. On 'Electronic Nose' methodology. Sensors and Actuators B: Chemical 204 (Supplement C), 2–17.

[6] Brenet, S., John-Herpin, A., Gallat, F.-X., Musnier, B., Buhot, A., Herrier, C., Rousselle, T., Livache, T., Hou, Y., Jul. 2018. Highly-Selective Optoelectronic Nose Based on Surface Plasmon Resonance Imaging for Sensing Volatile Organic Compounds. Analytical Chemistry.

[7] Brudzewski, K., Ulaczyk, J., Osowski, S., Markiewicz, T., Mar. 2007. Chiral behavior of TGS gas sensors: Discrimination of the enantiomers by the electronic nose. Sensors and Actuators B: Chemical 122 (2), 493–502.

[8] Di Carlo, S., Falasconi, M., 2012. Drift correction methods for gas chemical sensors in artificial olfaction systems: techniques and challenges. In: Advances in Chemical Sensors. InTech.

[9] Distante, C., Ancona, N., Siciliano, P., Jan. 2003. Support vector machines for olfactory signals recognition. Sensors and Actuators B: Chemical 88 (1), 30–39.

[10] Gaggiotti, S., Hurot, C., Weerakkody, J. S., Mathey, R., Buhot, A., Mascini, M., Hou, Y., Compagnone, D., 2020. Development of an optoelectronic nose based on surface plasmon resonance imaging with peptide and hairpin DNA for sensing volatile organic compounds. Sensors and Actuators B: Chemical 303.

[11] Hurot, C., Brenet, S., Buhot, A., Barou, E., Belloir, C., Briand, L., Hou, Y., 2019. Highly sensitive olfactory biosensors for the detection of volatile organic compounds by surface plasmon resonance imaging. Biosensors and Bioelectronics 123, 230–236.

[12] Khamis, S. M., Jones, R. A., Johnson, A. C., Preti, G., Kwak, J., Gelperin, A., 2012. DNA-decorated carbon nanotube-based FETs as ultrasensitive chemical sensors: Discrimination of homologues, structural isomers, and optical isomers. Aip Advances 2 (2), 022110.

[13] Kybert, N. J., Lerner, M. B., Yodh, J. S., Preti, G., Johnson, A. T. C., Mar. 2013. Differentiation of Complex Vapor Mixtures Using Versatile DNA–Carbon Nanotube Chemical Sensor Arrays. ACS Nano 7 (3), 2800–2807.

[14] Manoli, K., Magliulo, M., Torsi, L., 2013. Chiral Sensor Devices for Differentiation of Enantiomers. In: Schurig, V. (Ed.), Differentiation of Enantiomers II. Topics in Current Chemistry. Springer International Publishing, Cham, pp. 133–176.

[15] Marco, S., Jun. 2014. The need for external validation in machine olfaction: emphasis on health-related applications. Analytical and Bioanalytical Chemistry 406 (16), 3941–3956.

[16] Navarro-Sànchez, J., Argente-García, A. I., Moliner-Martínez, Y., Roca-Sanjuán, D., Antypov, D., Campíns-Falcó, P., Rosseinsky, M. J., Martí-Gastaldo, C., Mar. 2017. Peptide Metal–Organic Frameworks for Enantioselective Separation of Chiral Drugs. Journal of the American Chemical Society 139 (12), 4294–4297.

[17] Oh, E. H., Song, H. S., Park, T. H., May 2011. Recent advances in electronic and bioelectronic noses and their biomedical applications. Enzyme and Microbial Technology 48 (6), 427–437.

[18] Padilla, M., Perera, A., Montoliu, I., Chaudry, A., Persaud, K., Marco, S., Jan. 2010. Drift compensation of gas sensor array data by Orthogonal Signal Correction. Chemometrics and Intelligent Laboratory Systems 100 (1), 28–35.

[19] Pentsak, E. O., Eremin, D. B., Gordeev, E. G., Ananikov, V. P., Apr. 2019. Phantom Reactivity in Organic and Catalytic Reactions as a Consequence of Microscale Destruction and Contamination-Trapping Effects of Magnetic Stir Bars. ACS Catalysis 9 (4), 3070–3081.

[20] Persaud, K., Dodd, G., 1982. Analysis of discrimination mechanisms in the mammalian olfactory system using a model nose. Nature 299 (5881), 352–355.

[21] Raman, B., Stopfer, M., Semancik, S., Sep. 2011. Mimicking Biological Design and Computing Principles in Artificial Olfaction. ACS Chemical Neuroscience 2 (9), 487–499.

[22] Rudnitskaya, A., Sep. 2018. Calibration Update and Drift Correction for Electronic Noses and Tongues. Frontiers in Chemistry 6.

[23] Secundo, L., Snitz, K., Sobel, N., Apr. 2014. The perceptual logic of smell. Current Opinion in Neurobiology 25, 107–115.

[24] Tiwari, M. P., Prasad, A., Jan. 2015. Molecularly imprinted polymer based enantioselective sensing devices: A review. Analytica Chimica Acta 853, 1–18.

[25] Wasilewski, T., Gebicki, J., Kamysz, W., Jan. 2017. Bioelectronic nose: Current status and perspectives. Biosensors and Bioelectronics 87, 480–494.

[26] Wattanakit, C., Côme, Y. B. S., Lapeyre, V., Bopp, P. A., Heim, M., Yadnum, S., Nokbin, S., Warakulwit, C., Limtrakul, J., Kuhn, A., Feb. 2014. Enantioselective recognition at mesoporous chiral metal surfaces. Nature Communications 5, 3325.

[27] Yan, J., Guo, X., Duan, S., Jia, P., Wang, L., Peng, C., Zhang, S., 2015. Electronic Nose Feature Extraction Methods: A Review. Sensors 15 (11), 27804–27831.

[28] Zor, E., Morales-Narváez, E., Alpaydin, S., Bingol, H., Ersoz, M., Merkoçi, A., Jan. 2017. Graphene-based hybrid for enantioselective sensing applications. Biosensors and Bioelectronics 87, 410–416.

Supplementary materials
Reliable chiral recognition with an electronic nose

Pierre Maho, Cyril Herrier, Thierry Livache,
Guillaume Rolland, Pierre Comon, Simon Barthelmé

April 9, 2020

1 S1: Information about peptides

Cysteine N-term modified peptides (provided by Smartbioscience, France) are grafted on a gold-covered prism using thiol-gold bonding. The peptides are arrayed on the gold layer using a FlexArray S12 printer (Scienion, Germany) according to a process previously described ([1], [2]). The printed prisms are manufactured by batches of 25 pieces. Systematic quality controlled is carried out, using SPR measurement (image standardization) and by the measurement of the response generated by a known optical index shift. For this specific experiment, more than 2000 measurements can be performed without discrimination loss.

2 S2: Desorption phase

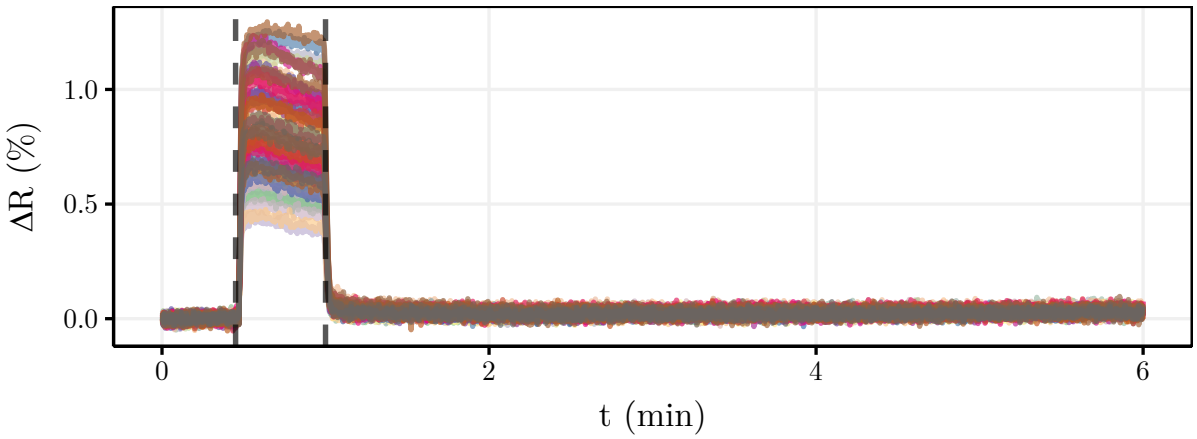

Figure 1: The time segmentation of each measurement is as follows: 30 sec for the reference gas (ie ambient air), 30 sec for analyte injection and 5 min for desorption. Here, we represent a complete measurement of (S)-Limonene.

3 S3: A linear model for concentration and normalization

In this supplementary material, we derive a theoretical model describing the instrument's response, which combines a model of the binding reaction and a model of Surface Plasmon Resonance imaging (SPRi). Under some assumptions, we show that the feature extracted is linearly dependent on the concentration of the gas, justifying the normalization we use.

The standard methodology for gas analysis with an eNose is a 3-phase injection: reference gas (here, ambient air), analyte (adsorption phase) and again reference gas (desorption phase). During the adsorption phase, a binding reaction occurs between the sensing material p and the analyte r. This reaction is governed by two parameters a_{pr} and d_{pr}, respectively the adsorption and desorption constant which are specific to the reaction:

$$\mathcal{A}_r + \mathcal{L}_p \underset{d_{pr}}{\overset{a_{pr}}{\rightleftharpoons}} \mathcal{A}_r\mathcal{L}_p$$

where $\mathcal{A}_r$ and $\mathcal{L}_p$ stand respectively for the analyte r and the sensing material p.

As explained in the main text, we use the entire adsorption phase by integrating over it. By noting t_s and t_e respectively the start and the end of the injection, the following feature x_{pr} is extracted from the time series $y_{pr}(t)$:

$$x_{pr} = \frac{1}{t_e - t_s} \int_{t_s}^{t_e} y_{pr}(t)\mathrm{d}t \tag{1}$$

Theoretically, $y_{pr}(t)$ can be modelled by combining a chemical model, describing the binding reaction, and a physical one, describing the transduction method (SPRi). We add that $y_{pr}(t)$ is the time series after reference subtraction.

3.1 Chemical model

A simple model of the sensing material is to view it as being composed of a number of sites $[\mathcal{L}_p]_s$ at the surface. These sites can potentially be occupied by the analyte $\mathcal{A}_r$ at a concentration $[\mathcal{A}](t) = c_r(t)$. We can describe the change in the number of occupied sites $[\mathcal{A}_r\mathcal{L}_p]_s$ by the differential equation:

$$\frac{\mathrm{d}[\mathcal{A}_r\mathcal{L}_p]_s(t)}{\mathrm{d}t} = a_{pr}c_r(t)\big([\mathcal{L}_p]_s - [\mathcal{A}_r\mathcal{L}_p]_s(t)\big) - d_{pr}[\mathcal{A}_r\mathcal{L}_p]_s(t) \tag{2}$$

where the equation only expresses the difference between the number of sites occupied at time t and the number of occupied sites becoming free at time t. This is referred to as the "Langmuir kinetics" [3]. (2) can be simplified to:

$$\frac{\mathrm{d}\theta_{pr}(t)}{\mathrm{d}t} = a_{pr}c_r(t)\big(1 - \theta_{pr}(t)\big) - d_{pr}\theta_{pr}(t) \tag{3}$$

where $\theta_{pr}(t) = \frac{[\mathcal{A}_r\mathcal{L}_p]_s}{[\mathcal{L}_p]_s}(t)$ stands for the fraction of sites occupied by the analyte $\mathcal{A}_r$ at time t. Due to the experimental setup, $c_r(t)$ can be approximated as a gate function:

$$c_r(t) = \begin{cases} c_r & \text{if } t \in [t_s, t_e] \\ 0 & \text{otherwise} \end{cases}$$

This leads to the following simplified equations:

Adsorption phase ($t \in [t_s, t_e]$)	Desorption phase ($t > t_e$)
$\frac{\mathrm{d}\theta_{pr}(t)}{\mathrm{d}t} = a_{pr}c_r\big(1 - \theta_{pr}(t)\big) - d_{pr}\theta_{pr}(t)$	$\frac{\mathrm{d}\theta_{pr}(t)}{\mathrm{d}t} = -d_{pr}\theta_{pr}(t)$

These differential equations when solved, lead to the following models

Adsorption phase ($t \in [t_s, t_e]$)	Desorption phase ($t > t_e$)
$\theta_{pr}(t) = \frac{a_{pr}c_r}{d_{pr} + a_{pr}c_r}(1 - \exp(-(d_{pr} + a_{pr}c_r)(t - t_s)))$	$\theta_{pr}(t) = \theta_{pr}(t_e)\exp(-d_{pr}(t - t_e))$

(4)

3.2 Physical model

The transduction method used is based on Surface Plasmon Resonance (SPR). We begin with a short introduction to SPR before going into models, and readers can find more details in [4].

SPR is the combination of two physical phenomena, namely two electromagnetic waves which exist under certain conditions. The first one is the surface plasmon (SP) which is an electromagnetic wave existing at any metal-dielectric interface. The second one is an evanescent wave created by an incident light which is totally reflected by a surface (meaning that the incidence angle is greater than the critical angle). This evanescent wave appears from both sides of the surface and decays exponentially in the direction perpendicular to the surface (it is thus limited to a given depth $L_z \approx 100$ nm). The conditions necessary to the creation of these two waves can be obtained by using a prism coated with gold and a monochromatic light. This system is represented in Figure 2a.

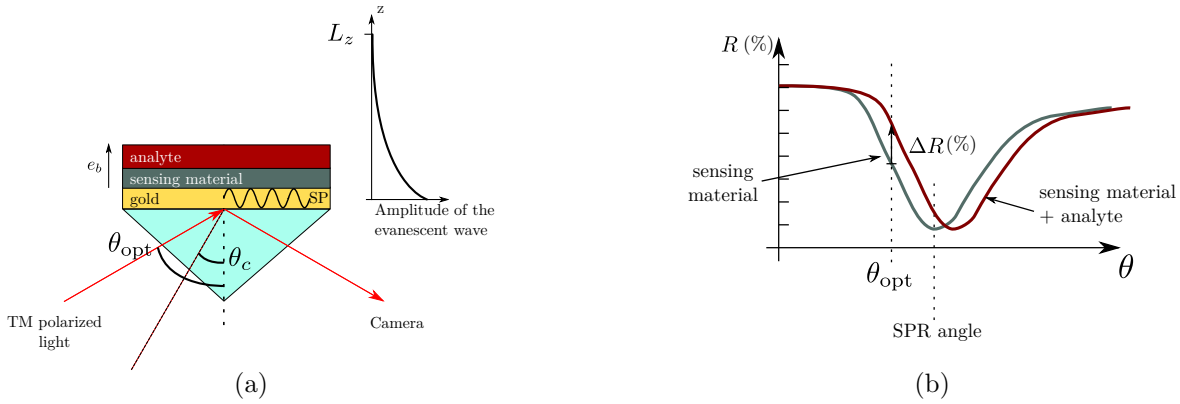

Figure 2: (a) SPRi system based on Kretschmann configuration (b) Plasmon curves. When an analyte binds to the sensing material, a shift in the plasmon curve occurs leading to an increase in reflectivity at the working angle θ_{opt}.

When the evanescent field is created by a TM-polarized (Transverse Magnetic) incident light, it can be used to excite the surface plasmons in a resonant manner. Here, the coupling of these two waves is performed by a change of the incidence angle. The resulting resonance of the surface plasmons generates a decrease in the amount of reflected light which is caught by a camera. By playing with this incidence angle, we can trace the reflectivity variations, leading to the plasmon curve represented in Figure 2b. This curve is minimal for a given angle, namely the SPR angle. The entire plasmon curve is quite sensitive to the medium near the metal interface. Indeed, any tiny increase in the refractive index of this layer will result in a simple shift to the right of the plasmon curve. Thus, when an analyte binds to the sensing material which is immobilized on the golden surface, the plasmon curve is shifted.

To quantify this shift (which lets us measure the interaction between sensing material and analyte), we set the incidence angle to θ_{opt}, located in the linear phase of the plasmon curve. The difference between the two values coming from the two plasmon curves (before, meaning the reference acquisition, and after the analyte injection) leads to our raw recording, namely ΔR (%). ΔR is dependent on the binding reaction occurring between the sensing material and the analyte and is related to the amount of adsorbed analytes.

To model ΔR as a function of adsorbed analytes, one can use Maxwell's equations, which leads to a complex model. However, this model can be well approximated in the liquid phase (and we assume that this model is still true in the gas phase) by a linear model, when the thickness e_b of the medium is much lower than the depth of the evanescent wave L_z [5, 6]:

$$\Delta R = \frac{S}{L_z}\frac{\partial n}{\partial C} \times \Gamma \tag{5}$$

where $S = \frac{\partial R}{\partial n}$ is the SPR sensitivity (the variation of reflectivity induced by a variation of refractive index), $\frac{\partial n}{\partial C}$ (cm^3/g) is the change in refractive index of the analyte with change in concentration and finally Γ (ng/mm^2) is the surface concentration of the analyte. To bring the fraction of occupied sites θ out, we rewrite Γ as $\Gamma = [\mathcal{L}]_s m\theta$ where m is the molecular mass of the analyte.

3.3 Physico-chemical model

In the following, we restore the previous subscripts to highlight each dimension of the problem. To highlight which parameter is dependent on the valve run (meaning the repetition of a given analyte), we incorporate this dimension in the subscript n. We describe the raw reflectivity $y_{prn}(t)$ as a function of the fraction of occupied sites as:

$$y_{prn}(t) = \beta S_p [\mathcal{L}_p]_s m_r \times \theta_{prn}(t) \tag{6}$$

where $\beta = \frac{1}{L_z}\frac{\partial n}{\partial C}$ is either dependent on SPR settings or approximately the same for all analytes. Since we are only interested in the adsorption phase, we can make the temporal model explicit (by incorporating (4) in (6)):

$$y_{prn}(t) = \beta S_p [\mathcal{L}_p]_s m_r \times \frac{a_{pr} c_{rn}}{d_{pr} + a_{pr} c_{rn}} (1 - \exp(-(d_{pr} + a_{pr} c_{rn})(t - t_s))) \tag{7}$$

3.4 Linearization

The feature defined by (1) is clearly non-linear as a function of the analyte concentration c_{rn}. To propose a simpler model, we assume that $\frac{a_{pr}}{d_{pr}} c_{rn} = k_{pr} c_{rn} \ll 1$ (which means that we are far from the saturation regime), which implies:

$$\begin{aligned}
x_{prn} &= \frac{\beta S_p [\mathcal{L}_p]_s m_r}{t_e - t_s} \int_{t_s}^{t_e} \frac{a_{pr} c_{rn}}{d_{pr} + a_{pr} c_{rn}} (1 - \exp(-(d_{pr} + a_{pr} c_{rn})(t - t_s)) \mathrm{d}t \\
&= \frac{\beta S_p [\mathcal{L}_p]_s m_r}{t_e - t_s} \int_{t_s}^{t_e} \frac{k_{pr} c_{rn}}{1 + k_{pr} c_{rn}} (1 - \exp(-d_{pr}(1 + k_{pr} c_{rn})(t - t_s)) \mathrm{d}t \\
&\approx \frac{\beta S_p [\mathcal{L}_p]_s m_r}{t_e - t_s} \int_{t_s}^{t_e} k_{pr} c_{rn} (1 - \exp(-d_{pr}(t - t_s)) \mathrm{d}t \\
&\approx \beta S_p [\mathcal{L}_p]_s m_r k_{pr} (1 - \frac{\exp(-d_{pr} t_e) - \exp(-d_{pr} t_s)}{d_{pr}(t_e - t_s)}) \times c_{rn} \\
&\approx k'_{pr} \times c_{rn}
\end{aligned} \tag{8}$$

3.5 Normalization

We remove c_{rn} contribution by log-transforming x_{prn} and centering across the spots which gives the normalized feature $\tilde{x}_{pr}$:

$$\log(x_{prn}) - \sum_{i=1}^{P} \log(x_{irn}) = \log(k'_{pr}) - \sum_{i=1}^{P} \log(k'_{ir}) + \cancel{\log(c_{rn})} - \cancel{\log(c_{rn})} = \tilde{x}_{pr} \tag{9}$$

It is interesting to note that the centering removes one degree of freedom, meaning that the signatures have no more P dimensions but in fact $P-1$ dimensions. This is explained by the linear dependency between the initial P dimensions created by the centering. This explains why we have only one feature remaining after normalization when we deal with a pair of sensing materials.

Eventually, even if this normalization removes a part of the time variation between the signatures, the correction is obviously not perfect and $\tilde{x}_{pr}$ is experimentally still dependent on n. This shows that all the assumptions which have led to the described model may not be all true, creating some drift (which is then corrected by another procedure).

4 S4: Controls of the empty setup

In the paper, some controls have been presented to reduce the possibility of an experimental bias. Here, we present two supplementary controls which were done in-between sessions.

First, the fluidic system is deliberately made in polyether ether ketone, a material which is assumed to be non-reactive with any analyte. However, any tiny residue stuck in the system could lead to a tiny difference between two lines, resulting a difference between two analytes. To remove this eventuality, we intensively checked the cleanliness of the whole fluidic system between Session 1 and Session 2. We ran 20 cycles without any vials. Then, we extracted from the signals the same feature as the one used in the study and described by (1). Since no vials were present, this value is expected to equal zero, meaning a clean line. This feature was not normalized to avoid any problems with negative values (the signal level was very low, and negative values could arise due to noise). We tested the discrimination between pairs of lines booked for a pair of enantiomers (line 2 against 4 and line 6 against 8). This test was as follows: first, we reduced dimensionality by taking the 3 first Principal Components, then performed a repeated 3-fold cross validation (repeated 50 times) with a linear Support Vector Machine from which we average the results to get an estimate of the classification rate between 2 empty lines. The results are reported in Figure 3 and show no discrimination due to a pollution in the lines. We highlight that the closer to 50% (chance rate) the results are, the better it is.

Second, the vials were either first-use, or intensively cleaned by rinsing them with acetone then ethanol and by drying them for several hours. However, as above, any tiny remaining pollutant in the vials could lead to a tiny discrimination between two vials, meaning between two analytes. Again, we carried out 20 cycles by placing empty vials and magnetic stir bars. The same discriminative analysis was repeated between pairs of vials booked for a pair of enantiomers. The results are reported in Figure 3 and show again no discrimination due to the vials.

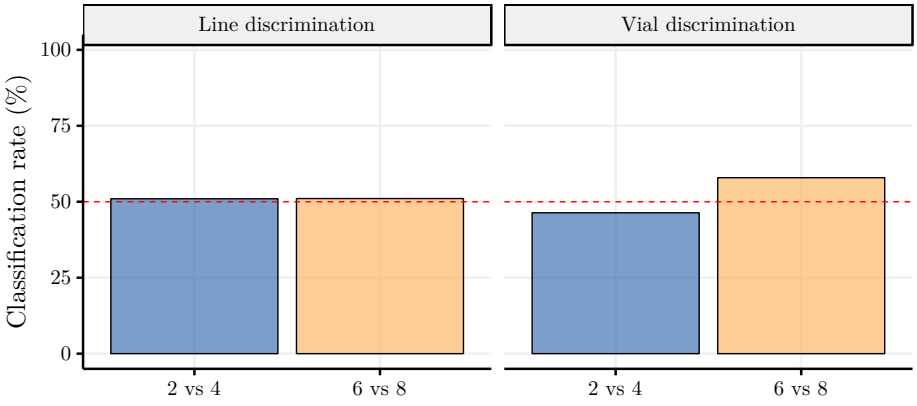

Figure 3: Discrimination power of the empty setup. Left facet checks if we can find any discrimination based only on gas lines. Right facet checks if we can find any discrimination only based on gas lines, empty vials and magnetic stir bars. The two isolated gas lines are the gas lines which are occupied by two different enantiomers (*eg* (R) and (S) carvone) during the experiments. A value close to 50% indicates that there is no discrimination.

References

[1] Yanxia Hou, Maria Genua, Dayane Tada Batista, Roberto Calemczuk, Arnaud Buhot, Pauline Fornarelli, Jamal Koubachi, David Bonnaffé, Els Saesen, Cédric Laguri, Hugues Lortat-Jacob, and Thierry Livache. Continuous evolution profiles for electronic-tongue-based analysis. *Angewandte Chemie International Edition*, 51(41):10394–10398, 2012.

[2] Sophie Brenet, Aurelian John-Herpin, François-Xavier Gallat, Benjamin Musnier, Arnaud Buhot, Cyril Herrier, Tristan Rousselle, Thierry Livache, and Yanxia Hou. Highly-Selective Optoelectronic Nose Based on Surface Plasmon Resonance Imaging for Sensing Volatile Organic Compounds. *Analytical Chemistry*, July 2018.

[3] A. Halperin, A. Buhot, and E. B. Zhulina. On the hybridization isotherms of DNA microarrays: the Langmuir model and its extensions. *Journal of Physics: Condensed Matter*, 18(18):S463, 2006.

[4] Jiri Homola, Sinclair S. Yee, and Günter Gauglitz. Surface plasmon resonance sensors: review. *Sensors and Actuators B: Chemical*, 54(1):3–15, January 1999.

[5] Esa Stenberg, Björn Persson, H\aa kan Roos, and Csaba Urbaniczky. Quantitative determination of surface concentration of protein with surface plasmon resonance using radiolabeled proteins. *Journal of colloid and interface science*, 143(2):513–526, 1991.

[6] Linda S. Jung, Charles T. Campbell, Timothy M. Chinowsky, Mimi N. Mar, and Sinclair S. Yee. Quantitative Interpretation of the Response of Surface Plasmon Resonance Sensors to Adsorbed Films. *Langmuir*, 14(19):5636–5648, September 1998.